ICESat-2 and Multispectral Images Based Coral Reefs Geomorphic Zone Mapping Using a Deep Learning Approach

Jing Zhong, Jie Sun, and Zulong Lai

***Abstract*—The coral reef geomorphic zone classification (CRGZC) map can provide a wealth of information for coastal management and protection. Remote sensing plays an important role in CRGZC by virtue of its speed, wide range, and low cost. Although many excellent results have been achieved in this field, there are still some shortcomings. With the development of machine learning, such methods are gradually introduced to CRGZC, yet the research and application of deep learning methods are still relatively few. In this article, based on ICESat-2 data and multispectral images, a deep learning model coupled with convolutional neural network (CNN) and random forest (RF) was proposed for coral reef geomorphic zone classification (CR_CRGZC). First, the priori bathymetry points were extracted from ICESat-2. Then, a near-shore bathymetry map was generated using a log-ratio model. Finally, topographic data and multispectral images were combined to achieve CRGZC through CR_CRGZC. The northeastern part of Coffin Island (CI) and the southern part of Punta Vaquero (PV) in Puerto Rico Island were selected as study areas. By comparing the classification results with those of CNN, RF, and maximum likelihood classification, CR_CRGZC outperformed the other classification methods. By quantitative analysis, the OA and Kappa coefficients of CR_CRGZC were 91.91% and 0.9013 in the CI region; and 89.91% and 0.8735 in the PV region, respectively. Under the same environmental requirements, this approach can map high-precision submeter CRGZC maps, providing a database for dynamic coral reef habitat mapping, which contributes to marine coastal ecosystem protection and coastal underwater topography monitoring.**

***Index Terms*—Coral reef geomorphic zone classification (CRGZC), deep learning, ICESat-2, multispectral image, nearshore bathymetry.**

I. Introduction

CORAL reefs are of great ecological and socio-economic importance. However, coral reefs are facing many threats, including climate change, marine pollution, and overfishing. These threats are harming marine life and their habitats, which in turn affects humans and the entire planet. Marine ecosystem assessments and ocean management are necessary to protect and preserve marine ecology, as well as for sustainable development of the oceans, monitoring of environmental changes in the oceans, and trends in the evolution of underwater structures. Coral reef geomorphic zone classification (CRGZC) maps provide effective tools for marine coastal ecosystem condition assessment and ocean management, which are of great economic value and environmental significance for humans [1]. CRGZC schemes are constantly evolving and increasing with human needs. The uncertainty of the scheme is due to the complexity of underwater geomorphology, the habitats of coral reefs, and the different roles of classification [2].

The classification and definition of coral reef geomorphology have been controversial since the beginning of modern scientific studies of the coral reef in the early 1980s. However, many attempts have been made to solve the problem of inconsistent classification schemes, a globally applicable or complete solution has not been found. This is the case because CRGZC schemes are influenced by the available knowledge and the practical context, and coral reef areas are multipurpose with studies that are closely related to multiple disciplines. At the same time, because of the complexity of coral reefs and the different roles of classification, no single CRGZC scheme can serve all researchers for their own particular purposes equally. Numerous CRGZC schemes have been developed, which are mainly constructed based on topography, species richness, and spatial coverage [3], [4]. To study the intrinsic properties of coral reef underwater discrete geomorphic zone systems, Short and Hesp [5], and Nordstrom [6] conducted thematic CRGZC. Maxwell [7] and Purkis et al. [8] classified marine coral reef ecosystems for monitoring marine coral reef ecosystems. Wright and Short [9], Masselink [10], and Nunn [11] implemented marine coral reef zone management and planning through CRGZC. Kendall [12], and Monaco et al. [13] developed special classification schemes in order to define and describe underwater benthic habitats of coral reefs. These classification schemes range from site-specific or subject-specific classification types to classification methods that cover large geographic areas [14], [15]. None of these CRGZC schemes are mutually exclusive, and they will overlap in some respects. Kendall [12], and Kennedy et al. [16] have proposed an ecological CRGZC scheme: the coral reef geomorphology always can be divided into Shoreline/Intertidal, Lagoon, Back reef, Reef crest, Fore reef, and Bank/shelf. Although this classification system is not a detailed classification of coral reef geomorphology in large biogeographic regions, this category is able to cover all topographic features of the marine coastal shallows, while

Manuscript received 26 June 2023; revised 28 January 2024; accepted 25 April 2024. Date of publication 6 May 2024; date of current version 23 May 2024. This work was supported by the National Natural Science Foundation of China under Grant 42171373. *(Corresponding author: Jie Sun.)*

The authors are with the School of Geography and Information Engineering, China University of Geosciences, Wuhan 430074, China (e-mail: jingzhong@cug.edu.cn; jiesun@cug.edu.cn; laizulong@cug.edu.cn).

Digital Object Identifier 10.1109/JSTARS.2024.3396374

having greater consistency. Based on the scheme, this article will provide a high-resolution, high-accuracy topographic database for the next step of a more detailed classification of coral reef benthic habitats.

In recent decades, optical, acoustic, and laser means have been used for CRGZC. The development of acoustic technology has provided advanced technical tools for classification [17], [18], [19]. Current CRGZC through acoustic techniques includes single-beam, side-scan sonar, and multibeam CRGZC. Despite the technical maturity and convenience of these methods for exploring coral reef geomorphology types, these acoustic detection systems need to be carried on platforms over water and at low altitudes for field detection, which makes it difficult for the acoustic techniques to perform field measurements in many shallow or area-constrained locations [20]. Airborne LiDAR has also been applied to CRGZC. In spite of the high accuracy and convenience of airborne LiDAR systems in acquiring coral reef geomorphology, they are not economical. Meanwhile, airborne LiDAR systems cannot perform field measurements in harsh environments and shallow or area-constrained locations [21]. Remote sensing images are widely used for CRGZC by their advantages of wide coverage, high timeliness, and independence from environmental and regional restrictions [22], [23]. Yet, it is difficult to adequately characterize the complex dynamic ecosystem of marine underwater using optical remote sensing imagery alone. Some research has shown that the combination of remote sensing data from multiple resources can increase the precision of CRGZC effectively [24], [25], [26]. In particular, underwater topographic data can compensate for the information of features that optical images cannot provide [27], hence underwater topographic data also play an important role in CRGZC.

Underwater topographic data are mainly extracted from bathymetry maps. Extracting underwater topography using existing bathymetry data would always face temporal resolution beyond the range of coral reef geomorphology changes, meanwhile, the spatial resolution is low, and the spatial resolution cannot be matched with optical images. Hence, in order to get a bathymetry map that meets the above-mentioned requirements, it is necessary to implement nearshore bathymetry. Active-passive fusion bathymetry is currently a predominant nearshore bathymetry method [28], [29], [30], where active bathymetry mainly relies on the in-situ bathymetry points provided by LiDAR. To break through the shortcomings of traditional airborne LiDAR such as expensive, low temporal resolution, and area limitation, scholars have tried to obtain bathymetry information using satellite-based LiDAR. Many scholars have found that satellite-based LiDAR can also be processed to extract the bathymetry points to meet people's needs. Therefore, extracting bathymetry points through a satellite-based LiDAR system gradually becomes an alternative method for nearshore bathymetry [31], [32], [33]. ICESat-2 is a space-borne system that uses a 531 nm photon-counting LiDAR with higher agility and underwater penetration [34]. The bathymetry points that meet the accuracy requirements can be quantitatively acquired from the ICESat-2 data after preprocessing and bathymetry error correction [35]. Simultaneously, the ICESat-2 interview cycle is 91 days, which can provide us with global underwater topographic data with a temporal resolution to classify coral reef geomorphology within the range of coral reef geomorphology changes. In the study, satellite-based ICESat-2 LiDAR and multispectral remote sensing images were employed to generate submeter coral reef bathymetry, from which topographic data are then extracted. The combination of topographic data and multispectral data provides sufficient features to achieve a highly accurate classification of coral reef geomorphology.

Machine learning was widely used for CRGZC. Mohamed et al. [36] used a combination of towed underwater cameras and high-resolution satellite images to achieve CRGZC through a support vector machine and K-nearest neighbor algorithm. Wicaksono et al. [37] and Burns et al. [38] extracted coral reef geomorphology from multispectral remote sensing imagery while discovering geomorphology changes over time based on general public machine learning algorithms. As deep learning evolves, deep learning has shown its superiority in CRGZC [39]. Fincham et al. [40] implemented CRGZC by convolutional neural networks (CNNs). Dang et al. [41] used traditional CNN to divide coral reef types along the coast of Vietnam. At present, deep learning has been used relatively few times in CRGZC. The majority of studies have extracted coral reef geomorphic zone categories from a single optical remote sensing image, ignoring the importance of topographic features in coral reef geomorphic zone categorization, which leads to relatively low accuracy in classifying coral reef underwater geomorphic zone features. In addition, conventional CNN tends to improve the accuracy of CRGZC by deepening the network structure. However, training complex network structures requires a lot of computational resources. Furthermore, deep learning models are susceptible to overfitting and lack of robustness, which are problems that need to be solved by current deep learning frameworks for coral reef geomorphic zone classification. CNN can effectively extract feature information from the images through convolutional layers, while random forest (RF) provides different interpretations of decision trees with better classification performance and lower computational cost. It has been shown that coupling CNN and RF can greatly simplify the structure of CNN and solve the problem of small-size images that cannot be downsampled multiple times, which can reduce the computational cost and improve the computational efficiency of the model[42], [43], [44]. Moreover, RF has a good classification performance to make up for the uncertainty and robustness of the CNN in classification effect [45]. Therefore, a deep learning-based classification model coupled with CNN and RF was proposed, which can combine the highly efficient capability of CNN for extracting features with the outstanding recognition capability of RF classifier.

In conclusion, this article proposed a deep learning model coupled with CNN and RF for CRGZC from ICESat-2 LiDAR and multispectral images. To begin with, bathymetry points obtained from ICESat-2 LiDAR were used as training samples for bathymetry inversion, and the traditional logarithmic ratio bathymetry inversion model [46] was applied to generate bathymetry maps of the two study areas. After that, underwater topographic features were extracted from the bathymetry maps. Then the combined features of multispectral images and topographic features were fed into CR_CRGZC for training with the

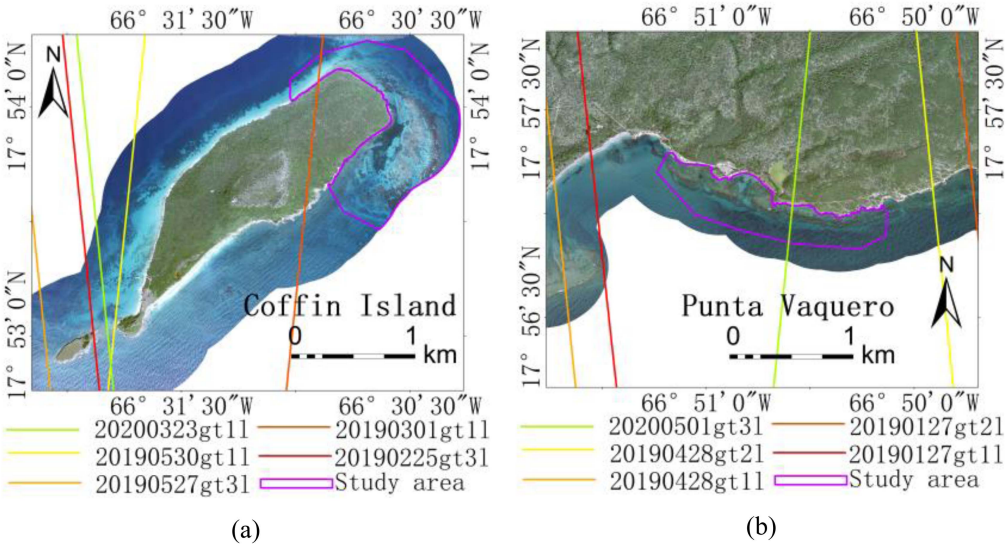

(a) (b)

Fig. 1. True color images of the south of Puerto Rico Island. (a) Northeast part of Coffin Island (CI). (b) South part of Punta Vaquero (PV). The color lines show the orbitals of ICESat-2 utilized in the study.

training samples. Finally, the trained model was used to generate CRGZC maps for the selected study areas. To quantitatively evaluate the classification accuracy of the method, the classical CNN, RF, and maximum likelihood classification (MLC) were selected as the baseline methods.

II. Data

A. High-Resolution Multispectral Images

With sensor development, an increasing number of satellite-based remote sensing images are available with submeter resolution and abundant wavebands, which provide strong support for bathymetry inversion and CRGZC. In this study, an open data source provided by the National Oceanic and Atmospheric Administration (NOAA [47]) was selected to simulate the high-resolution satellite remote sensing images dataset. The dataset was acquired by the Leica ADS40 digital sensor and geometrically corrected. The images of the dataset include four bands having a spatial resolution of 0.3 m: band 1 (blue), band 2 (green), band 3 (red), and band 4 (near infrared). The water column can absorb almost all of the incident energy of band 4 and reflect little energy. Therefore, band 4 should be avoided when performing underwater studies. Bands 1–3 can offer clear and abundant detailed underwater features, including information on the optical properties of different substrates on the bottom, water depth, and underwater topography. Two areas containing rich coral reef habitat types and complete coral reef geomorphic zone architecture were selected as study areas in the south of Puerto Rico Island. Fig. 1 shows true color images for two study areas (bands 1–3).

B. ICESat-2

In this article, the nearshore priori bathymetry training points were extracted from ICESat-2 relying on its excellent penetrating ability. The diameter of each footprint is 17 m and the spacing along the orbit is 0.7 m, which makes the spatial resolution of ICESat-2 sufficient for this study. Moreover, after the calibration, the obtained water depths in shallow and clear water areas can satisfy the accuracy requirements [35]. The ATL03 dataset includes height above the WGS 84 ellipsoid, latitude, longitude, and time and is the collection of all photons emitted by the Advanced Topographic Laser Altimeter System instrument on ICESat-2 observatory [48]. Each ATL03 data includes six pieces of ground laser tracks: gt1l, gt1r, gt2l, gt2r, gt3l, and gt3r. A strong signal track data and a weak signal track data overlap at the same laser track position to form a group of laser track data. Only the strong signal laser track data in each group was used in the study to achieve the extraction of bathymetry training points. The distribution of the used ATL03 laser tracks is shown in Fig. 1 and the track details are shown in Table I.

TABLE I
Nearshore Bathymetry LiDAR Data

Study Area	ICESat-2 laser track (Priori Bathymetry Points)	NOAA NGS Topobathy LiDAR (Validation Bathymetry Points)
Coffin Island	20200323gt1l	The dataset was acquired by a Riegl VQ-880-G II sensor [49].
	20190530gt1l	
Punta Vaquero	20190527gt3l	
	20190301gt1l	
	20190225gt3l	
	20200501gt3l	
	20190428gt2l	
	20190428gt1l	
	20190127gt2l	
	20190127gt1l	

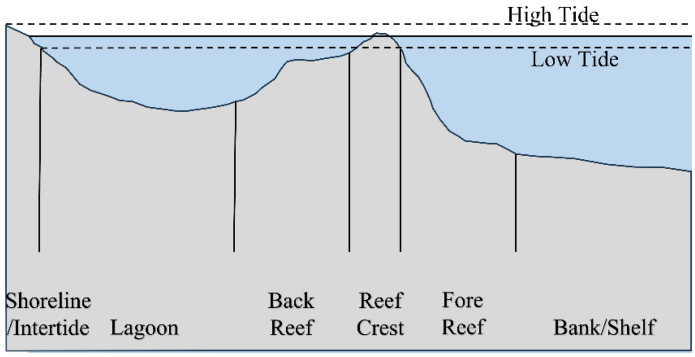

Fig. 2. Underwater topographic architecture transects.

C. Validation Data

1) Bathymetry Validation Data: In the study, topographic and bathymetry LiDAR data of coastal islands from NOAA [50] were used as validation bathymetry points. The vertical accuracy of this LiDAR bathymetry data can reach $((0.252) + (0.0075 \times d)^2)$ m (d represents the depth) in shallow water and $((0.302) + (0.013 \times d)^2)$ m in deep water at 95% confidence level. The information on the topographic LiDAR data from NOAA used in this article is shown in Table I.

2) Classification Validation Data: To accurately evaluate the accuracy of the CRGZC, the first-level classification result of the Puerto Rico Benthic Habitats Map and Geomorphic Zone Classification Map [51] was selected as our classification validation data. This data from both the geomorphic zone classification and the surface cover classification were carefully checked and plotted by a panel of experts while undergoing peer review. Since the sensor detection capability is limited underwater, six coral reef geomorphic zone categories were performed from the shoreline to the ocean shelf, as shown in Fig. 2. Six categories were classified from the shoreline to the ocean shelf including shoreline/intertidal, lagoon, back reef, reef crest, fore reef, and bank/shelf.

Shoreline/intertidal is the zone that lies between the highest water level that can be reached at high tide and the lowest water level at low tide. The lagoon is the sunken shallow water zone between the shoreline/intertidal, where the topography drops, and the back reef, where the topography rises. Due to the need to form a sunken zone, the presence of a lagoon must be accompanied by the presence of a raised and elevated reef crest. The back reef is the sloping slope of the transition from lagoon to reef crest. The reef crest is the flat protruding portion of the reef that can surface at low tide and can be clearly identified in multispectral remote sensing imagery. The fore reef is the sloping zone where the raised reef crest transitions to the flat and wide oceanic bank/shelf. The bank/shelf is the zone that extends from the fore reef to the deep sea to the continental cliffs, which is located in an open flat area with a moderate span of water depth. Fig. 2 and the above representations show that there is an obvious distinguishability of each coral reef geomorphic zone category in terms of underwater depth, slope, slope length, and so on. Therefore, the underwater topographic features such as water depth, slope, slope length, etc. are precisely used to better extract the underwater coral reef geomorphic zone types.

III. Methods

A. Method Overview

This study consists of the following key steps. At first, bathymetry points were retrieved from ICESat-2 data as a priori depth points for bathymetry inversion. Based on the bathymetry points, a bathymetry map was generated from the multispectral remote sensing images by the band log-ratio model. The bathymetry map was used for topographic analysis to generate the bathymetry digital elevation model (BDEM [52]), slope, aspect, length, and degree of relief (RFi [27]). Then the spectral information of multispectral images and topographic factors were combined to put into the classification framework (CR_CRGZC). Finally, the classification accuracy was evaluated with the classification validation data. Besides, to estimate the classification properties of the CR_CRGZC proposed in the study, conventional classification approaches such as MLC, CNN, and RF were employed as the baseline.

B. Extraction of Priori Bathymetry Points

There are five key steps to retrieve priori bathymetry points for bathymetry inversion from ICESat-2 as follows.

1) ICESat-2 LiDAR point cloud ellipsoidal height correction.
2) Sea level and seafloor were determined based on the confidence information and height of ICESat-2 LiDAR point cloud.
3) ICESat-2 LiDAR point cloud denoising based on the density-based spatial clustering of applications with noise method [53].
4) Seafloor points refraction correction [35].
5) Difference between the corrected height of the bottom point cloud and the height of the sea surface to obtain the prior depth points.

The comparison of ICESat-2 LiDAR point cloud bathymetry before and after processing is shown in Fig. 3.

Assuming that the topographic variability of the ocean bottom is negligible during the study years and only the tidal influence on the ocean bathymetry is taken into account, a temporal matching of multispectral data and ICESat-2 LiDAR data is required. The inverse bathymetry of multispectral images can be tidally corrected by mathematical expression (1) [54], [55]

$$H_{Image} = H_{Lidar} - \text{tide}_{Lidar} + \text{tide}_{Image}. \quad (1)$$

The equation above, H_{Image} is the instantaneous pixel bathymetry value for multispectral data acquisition; H_{Lidar} is the instantaneous bathymetry value extracted by ICESat-2 LiDAR; tide_{Lidar} represents the instantaneous tide value when ICESat-2 LiDAR was performing the information acquisition (tide_{Lidar} can be obtained by consulting the ICESat-2 track property value.); and tide_{Image} represents the instantaneous tide value when multispectral data were acquired, which can be

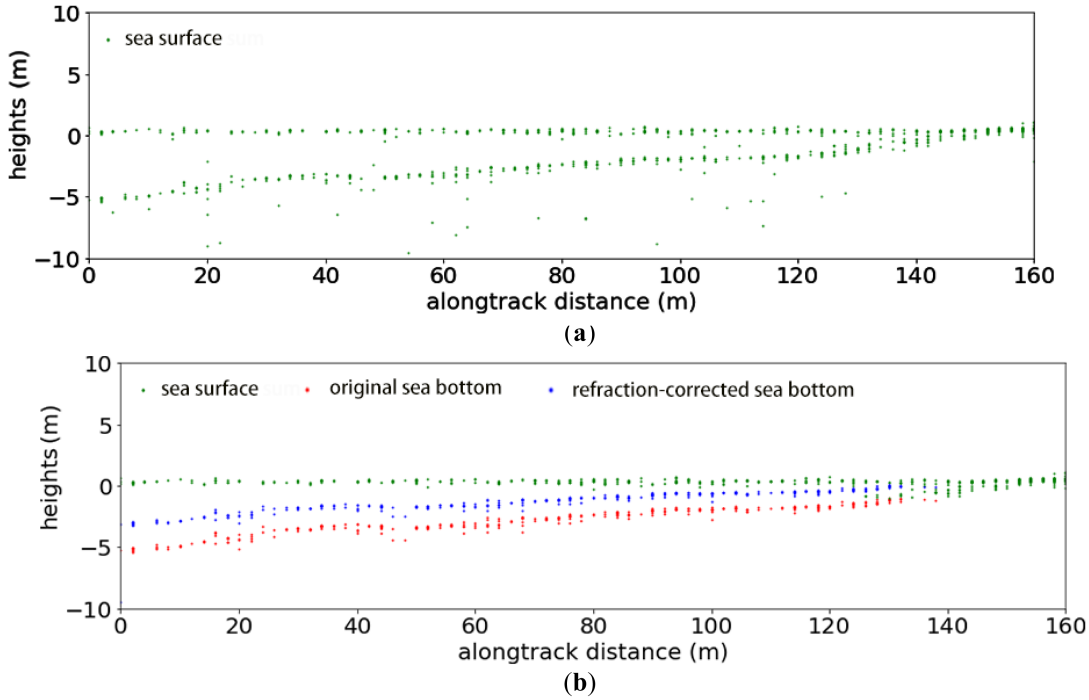

Fig. 3. Comparison of the original ICESat-2 LiDAR point cloud and the bathymetry processed ICESat-2 LiDAR point cloud. (a) Original ICESat-2 LiDAR point cloud. (b) Bathymetry processed ICESat-2 LiDAR point cloud.

viewed and corrected by the National Ocean Data Center [56] for the tidal information of the study area against the corresponding tide stations.

C. Bathymetry Inversion Model

The bathymetry inversion model adopted the traditional wave-band log-ratio model with the model mathematical expression shown in (2). The model is to establish a log-ratio relationship between the off-water reflectance of the two bands of the optical image first, then a linear model based on the log-ratio of the optical image bands and the priori bathymetry value is established.

$$\hat{H} = m_1 \frac{\ln(nR_B)}{\ln(nR_G)} - m_0 \tag{2}$$

where $\hat{H}$ denotes the priori bathymetry value; R_B and R_G are the off-water reflectances for optical images in the blue and green bands, respectively; m_0 represents the offset in the linear fit, m_1 denotes the fit coefficient of the linear fit between the log-ratio of optical image bands and the priori bathymetry value; and n is generally fixed to 1000, to make the logarithms all true and positive.

The multispectral remote sensing image was subjected to atmospheric correction and glare removal. Then the blue and green band values of the corresponding pixel points with the priori bathymetry points on the multispectral image were extracted to establish a log-ratio model. In the end, the corresponding preprocessed multispectral image bands were selected to calculate the band log-ratio values and to generate a bathymetry map at a high spatial resolution at 0.3 m by the established log-ratio model.

D. Deep Learning Model for CRGZC

Eight features were put into the model for training, including three multispectral bands (red, green, and blue) and five topographic features (BDEM, slope, aspect, length, and RFi).

CNN and RF are widely used in image classification and regression analysis. In the study, a coupled CNN and RF-based deep learning framework was designed for coral reef geomorphic zone classification (CR_CRGZC). There are few studies using coupled CNN and RF models for CRGZC applications. CNN can extract effective image features more efficiently, while RF solves the problem of small-size images that cannot be downsampled multiple times and provides different interpretations of decision trees with better classification performance and lower computational cost [45]. The deep learning framework (CR_CRGZC), shown in Fig. 4, used the convolution kernel and the nonlinear activation function. Rectified linear unit (ReLU) was selected as the activation function. The role of the convolution kernel is to retrieve the high-dimensional feature information from the image considering the local spatial correlation and to extend the feature information [57], [58]. ReLU is a nonlinear adjustment of the linear transformation between neurons [59]. ReLU calculation expression is shown in (3). The input feature tensor is transformed by $\mathrm{w}^{\mathrm{T}}x + \mathrm{b}$ and then by $\max(0, \mathrm{w}^{\mathrm{T}}x + \mathrm{b})$ transform as the input feature tensor for the next convolutional layer. The use of ReLU avoids the gradient explosion and gradient disappearance more effectively

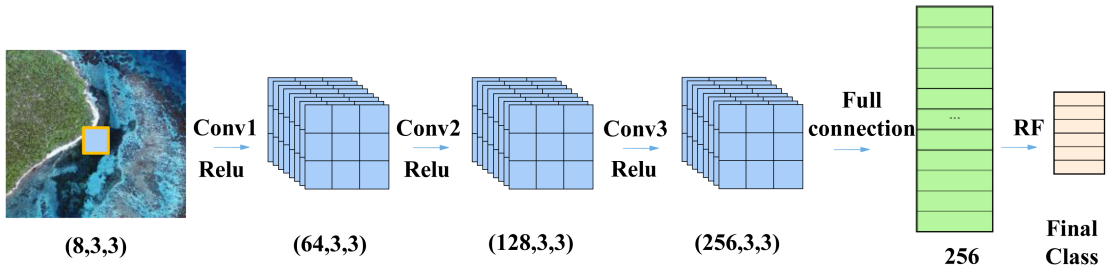

Fig. 4. CNN and RF fusion model (CR_CRGZC) architecture.

than the inverse gradient descent and backward propagation

$$f(x) = \max(0, x). \tag{3}$$

The equation above x is the independent variable of the entered network; $f(x)$ denotes the calculated value of the function.

The former part of the network consists of a classical CNN, including three convolutional layers containing 64, 128, and 256 neurons, respectively. ReLU was added between the two convolutional layers to nonlinearize the linear relationship. A fully connected layer (FC) followed the convolutional layer directly, with the output of the final classification results performed by the RF decision tree which provides different interpretations of decision trees with better classification performance and lower computational cost [42]. RF can greatly reduce the network structure of CNN [60], [61], [62]. Multiple downsampling is usually required to extract efficient feature information for image classification [63]. However, the input feature tensor is $8\times3\times3$, which cannot be downsampled multiple times. In the study, the RF decision tree was used to solve this problem and simplify the neural network structure. In addition, after the experiment, it was found that different RFs have robustness.

Three multispectral bands and five topographic factors were fused to generate eight bands of feature images. The classification sample points were extracted in the study area according to the prior knowledge to generate the classification a priori sample dataset. The feature tensors of size $8 \times 3 \times 3$ were fed to CR_CRGZC, with the classification category of the priori samples of CRGZC used as model training labels. Backpropagation was used together with the optimization method (Adaptive moment estimation, Adam) for network training. The loss function (CrossEntropyLoss) was used to calculate the loss values for the network classification. During training, the weights of the network were adjusted and refreshed based on the learning rate ($\alpha = 0.001$). Adam was then performed using gradient descent and iterated continuously. The model training epoch was set to 1000. Model training was completed when the model finished the training count while the loss function converged. The optimal model with the lowest error was determined as our model. The training dataset was input into the optimal model. After the FC, the $256 \times 3 \times 3$ three-dimensional (3-D) feature tensors were converted into 256 1-D feature tensors. The output feature tensors of the FC were input into the RF, which was used to achieve CRGZC. The output of CR_CRGZC was the total category of the classification.

E. Accuracy Evaluation

In the study, the root mean square error (RMSE) was selected to quantitatively assess the bathymetry inversion precision. RMSE can be used to determine the deviation of the model prediction value from the true value. A smaller RMSE indicates that the accuracy of the model bathymetry is higher. The coefficient of determination (R^2) is used to describe the fitting effect of the model. R^2 can also measure the degree of agreement in a regression model of the forecasted and true values. Generally, the bigger the R^2, the more well the model fits. The expressions of RMSE and R^2 are shown in (4) and (5)

$$\mathrm{RMSE} = \sqrt{\frac{1}{N}\sum_1^N \left(H_{\mathrm{Estimated}} - H_{\mathrm{Truth}}\right)^2} \tag{4}$$

$$R^2 = 1 - \frac{\sum_1^N \left(H_{\mathrm{Estimated}} - H_{\mathrm{Truth}}\right)^2}{\sum_1^N \left(\bar{H}_{\mathrm{Estimated}} - H_{\mathrm{Truth}}\right)^2} \tag{5}$$

where N indicates the number of samples at the validation bathymetry points; $H_{\mathrm{Estimated}}$ indicates the estimated bathymetry; $\bar{H}_{\mathrm{Estimated}}$ denotes the estimated average of bathymetry; and H_{Truth} indicates the airborne LiDAR bathymetry data provided by NOAA.

To quantitatively evaluate the precision of the proposed classification model (CR_CRGZC), MLC, RF, and CNN were employed in the comparison experiments, meanwhile, the overall classification accuracy (OA) and Kappa coefficient were used to measure the consistency among the CRGZC results from the proposed classification model and the classification validation data. Greater OA and Kappa coefficients indicate greater accuracy of model classification in the case of a randomly balanced distribution of samples. The OA and Kappa coefficients are calculated as shown in (6)–(8)

$$\mathrm{OA} = \frac{(\mathrm{TP} + \mathrm{TN})}{(\mathrm{TP} + \mathrm{TN} + \mathrm{FP} + \mathrm{FN})} \tag{6}$$

$$P_e = \frac{(\mathrm{TP}+\mathrm{FN}) \times (\mathrm{TP}+\mathrm{FP}) + (\mathrm{FN} + \mathrm{TN}) \times (\mathrm{TN} + \mathrm{FP})}{N^2} \tag{7}$$

$$\mathrm{Kappa} = \frac{P_0 - P_e}{1 - P_e}. \tag{8}$$

In the above-mentioned equation, TP indicates the true case; TN indicates the true counter case; FP indicates the false positive case; FN indicates the false counter case; N indicates the number

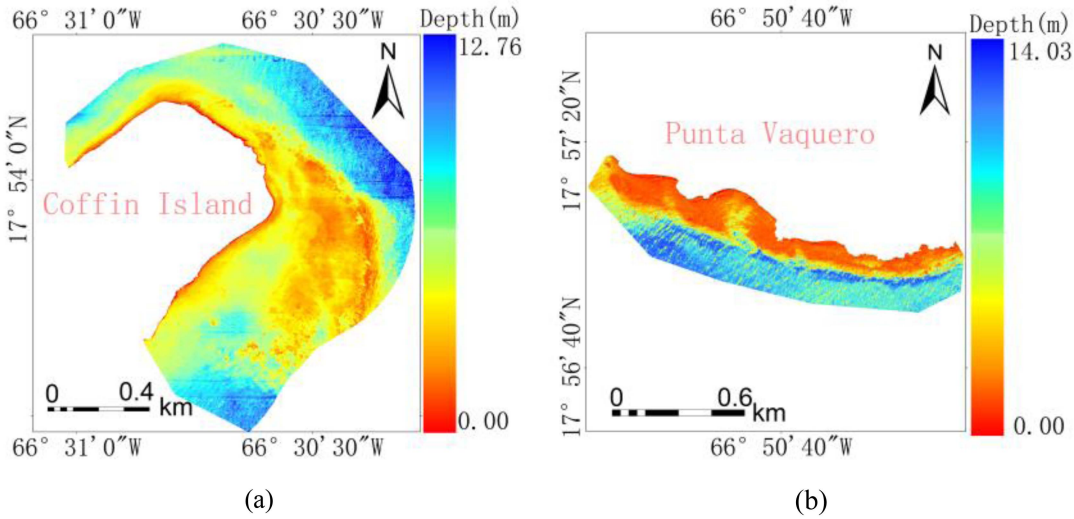

Fig. 5. Log-ratio model inversion bathymetry maps. (a) CI bathymetry. (b) PV bathymetry.

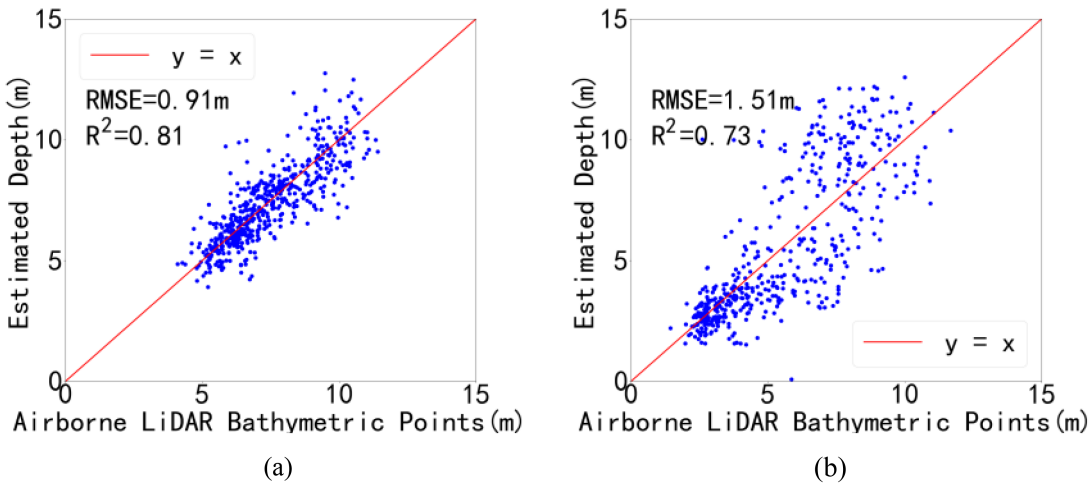

Fig. 6. Scatter plot measuring the correlation of the depth labels and estimated depths of the validation dataset for the bathymetry inversion. (a) Scatter plot of depth labels and estimated depths for the CI bathymetry validation dataset. (b) Scatter plot of depth labels and estimated depths for the PV bathymetry validation dataset.

of classification validation samples; and the value of P_0 is equal to the OA value.

IV. Experiment Results and Discussion

A. Bathymetry Maps of Models

The priori bathymetry points extracted by ICESat-2 were used to build a log-ratio model between multispectral remote sensing images and bathymetry. The fitted parameters $m1$ and $m0$ of the model at CI were -0.05 and 56.62, respectively. Meanwhile, the $m1$ and $m0$ at PV were -0.04 and 58.50, respectively. Then, the model was used to expand the point bathymetry information into a bathymetry map with the same spatial resolution as the multispectral images. As shown in Fig. 5, the bathymetry maps of CI and PV clearly show the distributions of bathymetry in space in both areas. The predicted maximum water depth in the CI area is 12.76 m. As the distance from the shoreline increases, the deepness of the CI slowly increases. The maximum predicted water depth in PV can reach 14.03 m. The water depth from near shore to far shore deepens sharply and then becomes shallow.

B. Accuracy Analysis of Bathymetry Estimates

The scatter plot shown in Fig. 6 depicts the correlation between the estimated bathymetry and the validated bathymetry. The model prediction accuracy was higher in the CI region with an RMSE of 0.91 m. The predicted and verified data had a strong correlation with an R^2 of 0.81, uniformly distributing on both sides of the $y = x$ line. In the PV region, with more dramatic water depth variations, bathymetry RMSE was 1.51 m and the accuracy of model prediction was lower. The estimated value deviated significantly from the true value, while the corresponding R^2 was only 0.73. The accuracy of bathymetry inversion

TABLE II
COMPARISON EXPERIMENTS OF DIFFERENT SIZES OF SUBIMAGES

Window size	0A(CI)	Kappa (CI)	OA(PV)	Kappa (PV)
1×1 pixels	86.29%	0.8532	80.68%	0.7916
2×2 pixels	90.15%	0.8872	87.19%	0.8518
3×3 pixels	**91.91%**	**0.9013**	**89.91%**	**0.8735**
4×4 pixels	89.64%	0.8814	85.38%	0.8483
5×5 pixels	87.28%	0.8626	80.03%	0.7894

The bold values indicate that classification works best.

TABLE III
COMPARISON EXPERIMENTS OF DIFFERENT FEATURE COMBINATIONS

Combination of Characteristic Factors	OA(CI)	Kappa (CI)	OA(PV)	Kappa (PV)
red、green、blue	80.19%	0.7986	77.89%	0.7526
red、green、blue、BDEM	87.67%	0.8677	84.91%	0.8385
red、green、blue、BDEM、slope	87.93%	0.8693	86.36%	0.8542
red、green、blue、BDEM、slope、aspect	88.19%	0.8814	87.02%	0.8674
red、green、blue、BDEM、slope、aspect、length	90.85%	0.8856	87.15%	0.8699
red、green、blue、BDEM、slope、aspect、length、RFi	**91.91%**	**0.9013**	**89.91%**	**0.8735**

The bold values indicate that classification works best.

decreases as the water depth deepens, while the complexity of the underwater topography also affects the bathymetry accuracy. Overall, the simple log-ratio model is capable of detecting shallow water depth effectively within the study area of this article.

C. Subimage Size Tuning

The size of the subimage directly affects the spatial feature information extracted by the convolution kernel. Excessively small subimages will ignore the geospatial coherence information, resulting in ineffective model fitting. Excessively large size leads to redundant feature information, excessive model training time, and model overfitting. Therefore, an appropriate image size should be selected. Table II shows the classification accuracy of CR_CRGZC using subimages of different sizes (with eight feature factors). After comparison, the 3 × 3 pixels window size had a relatively good performance.

D. Feature Factors Combination Tuning

The model training feature factors directly affect the classification accuracy. Insufficient feature factors cause the model unable to fit effectively, on the contrary, excessive feature factors cause the model to be overfitted and increase the time cost of model training. Table III shows the comparison accuracy of the model using different combinations of features for classification (using a 3 × 3 pixels size image). By comparing different combinations of feature factors, adding topographic feature factors to the red, green, and blue band features could quickly improve

TABLE IV
COMPARISON OF CLASSIFICATION ACCURACY FOR DIFFERENT CLASSIFICATION MODELS

	CR_CRGZC	MLC	CNN	RF
OA(CI)	**91.91%**	86.14%	76.32%	87.16%
Kappa (CI)	**0.9013**	0.8526	0.7525	0.8593
OA(PV)	**89.91%**	83.24%	72.75%	86.74%
Kappa (PV)	**0.8735**	0.8002	0.7018	0.8531

The bold values indicate that classification works best.

the model classification accuracy. Adding BDEM, slope, aspect, length, and RFi features to the three bands (red, green, blue), the OA of model classification improved by 11.72%% and 12.02% in CI and PV, respectively. By comparing the accuracy of several feature combinations listed in this article after model training it has been found that relatively higher classification accuracy can be obtained by utilizing eight features (red, green, blue, BDEM, slope, aspect, length, RFi). Consequently, the combination of eight feature factors for model training was used in the study.

E. CRGZC Map

The final CRGZC maps of the study area were generated as shown in Fig. 7. The comparison of the two study areas shows that CI has a complete set of six coral reef geomorphology categories, while PV lacks a back reef. The bathymetry map shown in Fig. 5 demonstrates that the underwater topography of PV is intensely changing, rising sharply to a reef crest after a wide and flat lagoon. Hence the lack of back reef transition. Comparing the four classification methods, the classification results showed obvious visual differences. The classification results of CR_CRGZC and RF were more uniform and complete without minor classification patches, while the MLC had obvious fine-grained classification results and CNN was not able to extract some categories completely. RF had the error of misclassifying the center of some categories and CRCZ made an improvement in this problem. In general, CR_CRGZC could extract the different categories of coral reef geomorphology more completely, simultaneously improving the problems of classification refinement and misclassification. In contrast, it appeared that the classification results of CNN differed significantly from the other three methods, mainly in the back reef of CI and the lagoon of PV. CNN was unable to accurately extract the back reef in the CI study area and the lagoon in the PV study area.

F. Accuracy Evaluation of CRGZC

To quantitatively assess the accurate qualification of the CR_CRGZC model, the OA and Kappa coefficients of the four classification methods of the two study areas were calculated, respectively, while the accuracy results of all classification methods are shown in Table IV.

From Table IV, it can be noticed that the accuracy of CR_CRGZC was the highest among the four classification methods in both study areas. The OA and Kappa coefficients of CR_CRGZC are 91.91% and 0.9013 in the CI region and 89.91% and 0.8735 in the PV region, respectively. CR_CRGZC improved OA by 5.77% and 4.67% over the commonly used MLC in the two study areas, respectively. CNN had the worst classification results in both study areas, whereas both MLC and RF classification accuracies were slightly lower than CR_CRGZC. Extracting high-dimensional feature information of images with CNN and then performing feature classification by RF could effectively improve the classification accuracy.

Comparing the classification accuracies of the two study areas, all four classification methods had higher classification accuracies in CI than in PV. There are two possible explanations for this phenomenon. First, the largest water depth attainable in the PV study area exceeds the largest water depth in the CI study area. As the depth of the water depth increases, the water column conditions become more complex. Therefore, bathymetry accuracy and CRGZC accuracy both decrease as the water depth increases. Second, dramatic underwater topographic changes and complex underwater overburden types can cause a decrease in classification accuracy. It is obvious from the bathymetry map that there are intense topographic changes in the direction of PV away from the coast, and also from the habitat classification map [50], it can be seen that the bottom cover type of the PV study area is more complex, which affects the accuracy of the classification.

Confusion matrices were generated by comparing the validation dataset classification labels with the CRGZC results of CR_CRGZC for each of the two study regions, and the confusion matrices are shown in Fig. 8. The distribution of misclassifications can be seen in Fig. 8. In both study areas shoreline/intertidal could be accurately classified, with comparatively obvious misclassification between all other coral reef geomorphology categories. The lack of a back reef transition between PV's submerged lagoon and reef crest and the intense topographic variation make it easier to confuse the two categories when they border each other.

G. Error Analysis of CRGZC

CRGZC error sources in the study mainly include bathymetry maps, multispectral images, and the validation dataset of CRGZC.

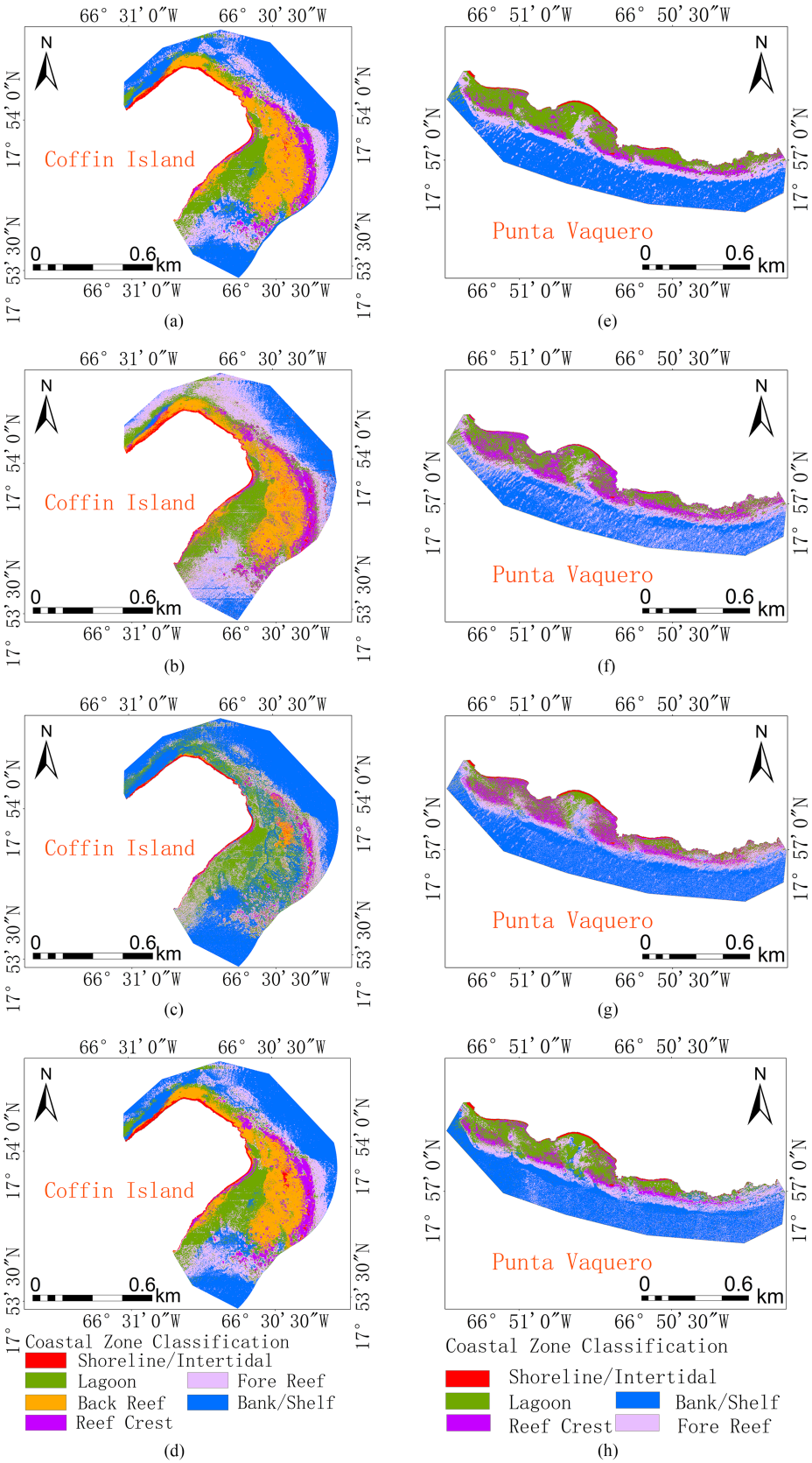

Fig. 7. CRGZC maps. (a)–(d) CRGZC maps of CI obtained by CR_CRGZC, MLC, CNN, and RF, respectively. (e)–(g) are the CRGZC maps of PV obtained by CR_CRGZC, MLC, CNN, and RF, respectively.

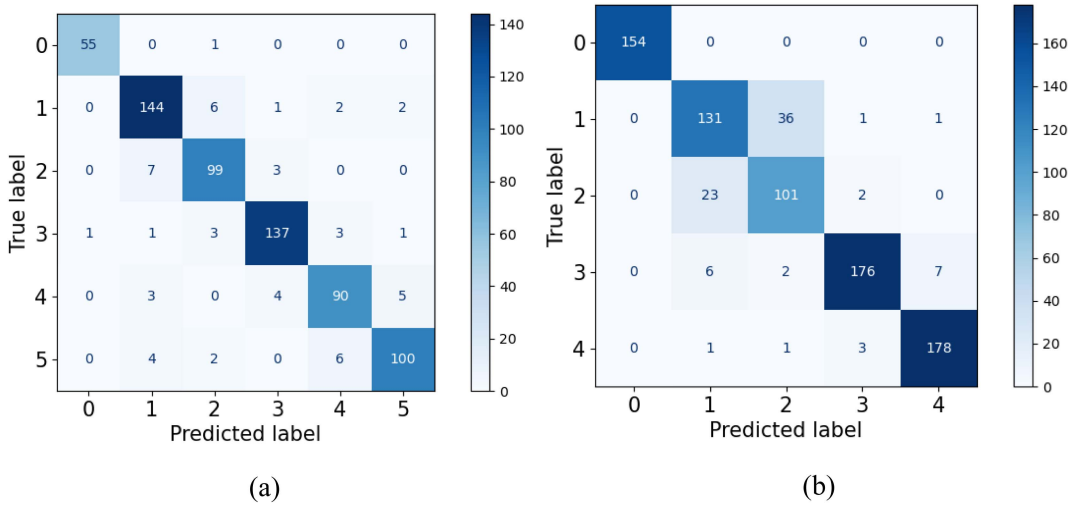

Fig. 8. Confusion matrix calculated by the labels of the validation dataset and the results of CRGZC. 0-5 of Fig. 8 indicate shoreline/intertidal, lagoon, back reef, reef crest, fore reef, and bank/shelf, respectively. (a) Confusion matrix for CI and (b) Confusion matrix for PV.

The error of the bathymetry map leads to the error of CRGZC. First, the extraction of bathymetry points from ICESat-2 eliminated most of the errors after some preprocessing work, but the effect of the refractive index of the water body still led to the error of the bathymetry map [64]; meanwhile, due to the noise and multipath effects, the processed sea level and bottom of the sea both have a certain thickness, as shown in Fig. 2, which also generates bathymetry maps with errors; finally, in-situ bathymetry points were employed as validation dataset in bathymetry inversion, but it is difficult to keep in-situ bathymetry points and optical images synchronized in time, by which the in-situ bathymetry data precision can also be influenced by geographic position, ocean tides, and collection methods. Overall, the above-mentioned three aspects can produce errors on bathymetry maps, which lead to errors in CRGZC.

Although the multispectral remote sensing images were preprocessed with atmospheric correction and flare removal, small amounts of clouds and solar flares are still present in some regions. At the same time, waves will also be present in some reef crest regions. These errors in the images may lead to classification errors [65]. In addition, water properties, water turbidity, submerged geomorphology, and complex submerged coverage types could also impact the classification precision [66], [67], [68].

The validation data span a large period of time from other remote sensing data. Although some methods are used to reduce errors, changes in underwater topography, ocean tides, and the accuracy of validation data can introduce errors [30].

H. Transferability of CR_CRGZC

The transferability of the model proposed in this article was verified using the ground truth field data for CRGZC provided by Roelfsema (Access to the data can be accessed Online).[1]

[1][Online]. Available at: https://figshare.com/collections/Benthic_and_Geomorphic_Reference_Data_for_Global_Coral_Reef_Mapping/.

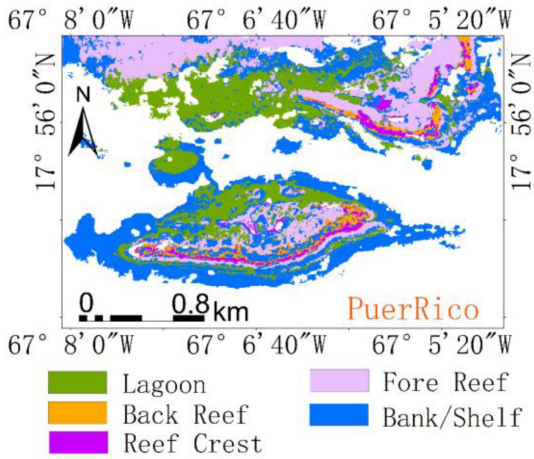

Fig. 9. CRGZC maps of PR island obtained by CR_CRGZC.

Due to the limitation of ground truth field data, a limited area of fringing reefs in the southwest of Puer Rico (PR) island was selected. The CRGZC map obtained by CR_CRGZC is shown in Fig. 9. From the figure, it can be seen that the model proposed in this article is able to completely extract the coral reef geomorphic zone types in the region. At the same time, the accuracy of CRGZC was assessed based on the ground truth field data and the results are shown in Table V. From the table, it can be seen that the CR_CRGZC has higher accuracy in classifying coral reef geomorphic zones in the PR study area. As a whole, it seems that CR_CRGZC proposed in this article enables the classification of coral reef geomorphic zones more accurately and has a certain degree of transferability. At the same time, the finding also suggested that the CRGZC scheme proposed by Kendall is also applicable to fringing reefs with similar geomorphic distribution.

TABLE V
CLASSIFICATION ACCURACY COMPARED TO GROUND TRUTH FIELD DATA

	OA(PR)	Kappa (PR)
CR_CRGZC	**90.54%**	**0.8799**
MLC	77.48%	0.7139
CNN	73.81%	0.6813
RF	82.13%	0.7728

The bold values indicate that classification works best.

V. CONCLUSION AND PROSPECT

In this article, we proposed a deep learning framework with coupled CNN and RF for CR_CRGZC. Initially, bathymetry maps of the study areas were produced using priori bathymetry points extracted from ICESat-2 LiDAR data and multispectral images. Then topographic analysis was performed based on the bathymetry map. Both multispectral images and topographic features were used for the training of the CR_CRGZC. At last, the CRGZC map of the study area was mapped by the optimal trained model. The MLC, CNN, and RF were used for the comparison experiments. It could be seen from the classification results that CR_CRGZC had better coherence and completeness. Simultaneously, CR_CRGZC improved the finesse of classification results of other methods.

To quantitatively assess the precision of CR_CRGZC, the CRGZC results of CR_CRGZC were compared with the CRGZC maps from NOAA. The comparison revealed that the CR_CRGZC classification accuracy was significantly higher than the other three classification methods. The OA and Kappa coefficients of CR_CRGZC were 91.91% and 0.9013 in the CI region and 89.91% and 0.8735 in the PV region, respectively. The CNN classification accuracy was the lowest, whereas the RF classification accuracy was slightly higher than the MLC.

The confusion matrix of CRGZC results of CR_CRGZC suggested that it was difficult to find regularity in misclassification. Comparing the CRGZC results of CI and PV study areas, the CRGZC accuracy of CR_CRGZC was found to decrease with increasing water depth, as well as drastic topographic changes and complex topography would reduce the classification accuracy. Using ground truth data of CRGZC to validate that the model has a certain degree of transferability.

We are eager to test with more datasets to propose classification models with higher robustness and apply them to high accuracy global scale and multitemporal CRGZC. Meanwhile, these highly accurate CRGZC maps will be useful for coral reef resource development, underwater geological structure, and environmental change monitoring.

Coral reef underwater plant and animal habitats are mainly distributed within specific coral reef underwater zone areas, so accurate CRGZC results can help us better understand the distribution and characteristics of underwater plant and animal habitats. The scholars used the CRGZC maps as first-level classification maps and based on these, second-level coral reef underwater habitat maps were developed. Consequently, the inclusion of high-precision coral reef geomorphic zone features in habitats classification is eager to increase the accuracy of coral reef underwater habitats classification.

ACKNOWLEDGMENT

The authors would like to thank the NOAA for high-resolution satellite remote sensing data and topographic and bathymetry LiDAR data of coastal islands, the National Centers for Coastal Ocean Science for the Puerto Rico Benthic Habitats Map and Geomorphic Zone Classification Map, and the Goddard Space Flight Center for distributing the ICESat-2 data, besides, the authors also thank the editors and reviewers for their detailed comments and efforts toward improving the study.

REFERENCES

[1] C. Roelfsema et al., "Coral reef habitat mapping: A combination of object-based image analysis and ecological modeling," *Remote Sens. Environ.*, vol. 208, pp. 27–41, 2018.
[2] R. A. Davis Jr and M. O. Hayes, "What is a wave-dominated coast?," *Developments Sedimentol.*, vol. 39, pp. 313–329, 1984.
[3] W. M. Goldberg, "The ecology of the coral-octocoral communities off the southeast Florida coast: Geomorphology, species composition, and zonation," *Bull. Mar. Sci.*, vol. 23, pp. 465–488, 1973.
[4] Y. Loya, "Community structure and species diversity of hermatypic corals at Eilat, Red sea," *Mar. Biol.*, vol. 13, pp. 100–123, 1972.
[5] A. D. Short and P. A. Hesp, "Wave, beach and dune interactions in southeastern Australia," *Mar. Geol.*, vol. 48, pp. 259–284, 1982.
[6] K. Nordstrom, "The intrinsic characteristics of depositional coastal landforms," *Geographical Rev.*, vol. 80, pp. 68–81, 1990.
[7] W. G. H. Maxwell, "Atlas of the great barrier reef," 1968.
[8] S. J. Purkis et al., "High-resolution habitat and bathymetry maps for 65,000 sq. km of Earth's remotest coral reefs," *Coral Reefs*, vol. 38, pp. 467–488, 2019.
[9] L. D. Wright and A. D. Short, "Morphodynamic variability of surf zones and beaches: A synthesis," *Mar. Geol.*, vol. 56, pp. 93–118, 1984.
[10] G. Masselink, "The effect of tides on beach morphodynamics," in *Handbook of Beach and Shoreface Morphodynamics*. Hoboken, NJ, USA: Wiley, 1999, pp. 204–229.
[11] P. D. Nunn, "Sea-level changes over the past 1,000 years in the Pacific," *J. Coastal Res.*, vol. 9, pp. 23–30, 1998.
[12] M. S. Kendall, "Methods used to map the benthic habitats of Puerto Rico and the US Virgin Islands," 2002.
[13] M. E. Monaco et al., "National summary of NOAA's shallow-water benthic habitat mapping of US coral reef ecosystems," 2012.
[14] S. O. Carroll, "Coastal erosion and shoreline classification in Stratford," Prince Edward Island Dept. Environ., Prince Edward Island, Charlottetown, PE, Canada, Tech. Rep., p. 96, 2010.
[15] P. Athanasiou, A. Van Dongeren, A. Giardino, M. Vousdoukas, S. Gaytan-Aguilar, and R. Ranasinghe, "Global distribution of nearshore slopes with implications for coastal retreat," *Earth System Sci. Data*, vol. 11, pp. 1515–1529, 2019.
[16] E. V. Kennedy et al., "Reef cover, a coral reef classification for global habitat mapping from remote sensing," *Sci. Data*, vol. 8, 2021, Art. no. 196.
[17] C. J. Brown and P. Blondel, "Developments in the application of multibeam sonar backscatter for seafloor habitat mapping," *Appl. Acoust.*, vol. 70, pp. 1242–1247, 2009.
[18] M. Kang, T. Nakamura, and A. Hamano, "A methodology for acoustic and geospatial analysis of diverse artificial-reef datasets," *ICES J. Mar. Sci.*, vol. 68, pp. 2210–2221, 2011.
[19] R. J. Kloser, J. D. Penrose, and A. J. Butler, "Multi-beam backscatter measurements used to infer seabed habitats," *Continental Shelf Res.*, vol. 30, pp. 1772–1782, 2010.
[20] R. Schwarz, G. Mandlburger, M. Pfennigbauer, and N. Pfeifer, "Design and evaluation of a full-wave surface and bottom-detection algorithm for LiDAR bathymetry of very shallow waters," *ISPRS J. Photogrammetry Remote Sens.*, vol. 150, pp. 1–10, 2019.
[21] V. Klemas, "Beach profiling and LIDAR bathymetry: An overview with case studies," *J. Coastal Res.*, vol. 27, pp. 1019–1028, 2011.

[22] F. Eugenio, J. Marcello, and J. Martin, "High-resolution maps of bathymetry and benthic habitats in shallow-water environments using multispectral remote sensing imagery," *IEEE Trans. Geosci. Remote Sens.*, vol. 53, no. 7, pp. 3539–3549, Jul. 2015.

[23] S. Cerdeira-Estrada et al., "Benthic habitat and bathymetry mapping of shallow waters in puerto morelos reefs using remote sensing with a physics based data processing," in *Proc. IEEE Int. Geosci. Remote Sens. Symp.*, 2012, pp. 4383–4386.

[24] D. J. Barnes, "Perspectives on coral reefs," 1983.

[25] A. Minghelli et al., "Estimation of bathymetry and benthic habitat composition from hyperspectral remote sensing data (BIODIVERSITY) using a semi-analytical approach," *Remote Sens.*, vol. 13, 2021, Art. no. 1999.

[26] C. Roelfsema, S. Phinn, S. Jupiter, J. Comley, and S. Albert, "Mapping coral reefs at reef to reef-system scales, 10s–1000s km2, using object-based image analysis," *Int. J. Remote Sens.*, vol. 34, pp. 6367–6388, 2013.

[27] A. L. Quilleuc, A. Collin, M. F. Jasinski, and R. Devillers, "Very high-resolution satellite-derived bathymetry and habitat mapping using pleiades-1 and ICESat-2," *Remote Sens.*, vol. 14, 2022, Art. no. 133.

[28] X. Zhang et al., "Nearshore bathymetry based on ICESat-2 and multispectral images: Comparison between sentinel-2, landsat-8, and testing Gaofen-2," *IEEE J. Sel. Topics Appl. Earth Observ. Remote Sens.*, vol. 15, pp. 2449–2462, 2022.

[29] A. Pacheco, J. Horta, C. Loureiro, and Ó. Ferreira, "Retrieval of nearshore bathymetry from Landsat 8 images: A tool for coastal monitoring in shallow waters," *Remote Sens. Environ.*, vol. 159, pp. 102–116, 2015.

[30] I. Caballero and R. P. Stumpf, "Retrieval of nearshore bathymetry from Sentinel-2A and 2B satellites in south florida coastal waters," *Estuarine, Coastal Shelf Sci.*, vol. 226, 2019, Art. no. 106277.

[31] Y. Ma et al., "Satellite-derived bathymetry using the ICESat-2 lidar and Sentinel-2 imagery datasets," *Remote Sens. Environ.*, vol. 250, 2020, Art. no. 112047.

[32] D. Zhang, Y. Chen, Y. Le, Y. Dong, G. Dai, and L. Wang, "Refraction and coordinate correction with the JONSWAP model for ICESat-2 bathymetry," *ISPRS J. Photogrammetry Remote Sens.*, vol. 186, pp. 285–300, 2022.

[33] B. J. Babbel, C. E. Parrish, and L. A. Magruder, "ICESat-2 elevation retrievals in support of satellite-derived bathymetry for global science applications," *Geophysical Res. Lett.*, vol. 48, 2021, Art. no. e2020GL090629.

[34] T. Markus et al., "The Ice, cloud, and land elevation Satellite-2 (ICESat-2): Science requirements, concept, and implementation," *Remote Sens. Environ.*, vol. 190, pp. 260–273, 2017.

[35] C. E. Parrish, L. A. Magruder, A. L. Neuenschwander, N. Forfinski-Sarkozi, M. Alonzo, and M. Jasinski, "Validation of ICESat-2 ATLAS bathymetry and analysis of ATLAS's bathymetric mapping performance," *Remote Sens.*, vol. 11, 2019, Art. no. 1634.

[36] H. Mohamed, K. Nadaoka, and T. Nakamura, "Assessment of machine learning algorithms for automatic benthic cover monitoring and mapping using towed underwater video camera and high-resolution satellite images," *Remote Sens.*, vol. 10, 2018, Art. no. 773.

[37] P. Wicaksono, P. A. Aryaguna, and W. Lazuardi, "Benthic habitat mapping model and cross validation using machine-learning classification algorithms," *Remote Sens.*, vol. 11, 2019, Art. no. 1279.

[38] C. Burns, B. Bollard, and A. Narayanan, "Machine-learning for mapping and monitoring shallow coral reef habitats," *Remote Sens.*, vol. 14, 2022, Art. no. 2666.

[39] A. Clark, B. Moorman, D. Whalen, and G. Vieira, "Multiscale object-based classification and feature extraction along arctic coasts," *Remote Sens.*, vol. 14, 2022, Art. no. 2982.

[40] J. I. Fincham, C. Wilson, J. Barry, S. Bolam, and G. French, "Developing the use of convolutional neural networking in benthic habitat classification and species distribution modelling," *ICES J. Mar. Sci.*, vol. 77, pp. 3074–3082, 2020.

[41] K. B. Dang, Q. T. Bui, and T. P. N. Pham, "A convolutional neural network for coastal classification based on ALOS and NOAA satellite data," *IEEE Access*, vol. 8, pp. 11824–11839, 2020.

[42] G. Kwak, C. Park, K. Lee, S. Na, H. Ahn, and N. Park, "Potential of hybrid CNN-RF model for early crop mapping with limited input data," *Remote Sens.*, vol. 13, 2021, Art. no. 1629.

[43] S. Yang, L. Gu, X. Li, T. Jiang, and R. Ren, "Crop classification method based on optimal feature selection and hybrid CNN-RF networks for multi-temporal remote sensing imagery," *Remote Sens.*, vol. 12, 2020, Art. no. 3119.

[44] G. Kwak, C. Park, K. Lee, S. Na, H. Ahn, and N. Park, "Potential of hybrid CNN-RF model for early crop mapping with limited input data," *Remote Sens.*, vol. 13, 2021, Art. no. 1629.

[45] S. Yang, L. Gu, X. Li, T. Jiang, and R. Ren, "Crop classification method based on optimal feature selection and hybrid CNN-RF networks for multi-temporal remote sensing imagery," *Remote Sens.*, vol. 12, 2020, Art. no. 3119.

[46] R. P. Stumpf, K. Holderied, and M. Sinclair, "Determination of water depth with high-resolution satellite imagery over variable bottom types," *Limnol. Oceanogr.*, vol. 48, pp. 547–556, 2003.

[47] Y. Liu, Q. Guan, and X. Zhao, "Copy-move forgery detection based on convolutional kernel network," *Multimedia Tools Appl.*, vol. 77, pp. 18269–18293, 2018.

[48] T. A. Neumann et al., *ATLAS/ICESat-2 L2A Global Geolocated Photon Data, Version 3*. Boulder, CO, USA: NASA National Snow and Ice Data Center Distributed Active Archive Center, 2020.

[49] Y. Yaakoubi, F. Soumis, and S. Lacoste-Julien, "Structured convolutional kernel networks for airline crew scheduling," in *Proc. Int. Conf. Mach. Learn.*, 2021, pp. 11626–11636.

[50] D. Chen, L. Jacob, and J. Mairal, "Biological sequence modeling with convolutional kernel networks," *Bioinformatics*, vol. 35, pp. 3294–3302, 2019.

[51] Z. Li, F. Liu, W. Yang, S. Peng, and J. Zhou, "A survey of convolutional neural networks: Analysis, applications, and prospects," *IEEE Trans. Neural Netw. Learn. Syst.*, vol. 33, no. 12, pp. 6999–7019, Dec. 2022.

[52] R. R. Rodriguez, *Integration of Topographic and Bathymetric Digital Elevation Model Using ArcGIS Interpolation Methods: A Case Study of the Klamath River Estuary*. Los Angeles, CA, USA: Univ. Southern California, 2014.

[53] D. Birant and A. Kut, "ST-DBSCAN: An algorithm for clustering spatial–temporal data," *Data Knowl. Eng.*, vol. 60, pp. 208–221, 2007.

[54] T. K. Holland, "Application of the linear dispersion relation with respect to depth inversion and remotely sensed imagery," *IEEE Trans. Geosci. Remote Sens.*, vol. 39, no. 9, pp. 2060–2072, Sep. 2001.

[55] Z. Lee, C. Hu, R. Arnone, and Z. Liu, "Impact of sub-pixel variations on ocean color remote sensing products," *Opt. Exp.*, vol. 20, pp. 20844–20854, 2012.

[56] J. Wu, "Introduction to convolutional neural networks," *Nat. Key Lab Novel Softw. Technol. Nanjing Univ.*, vol. 5, 2017, Art. no. 495.

[57] J. Mairal, P. Koniusz, Z. Harchaoui, and C. Schmid, "Convolutional kernel networks," in *Proc. Adv. Neural Inf. Process. Syst.*, 2014, Art. no. 27.

[58] A. Moschitti, "Efficient convolution kernels for dependency and constituent syntactic trees," in *Proc. 17th Eur. Conf. Mach. Learn.*, 2006, pp. 318–329.

[59] A. F. Agarap, "Deep learning using rectified linear units (relu)," 2018, *arXiv:1803.08375*.

[60] F. Khozeimeh et al., "RF-CNN-F: Random forest with convolutional neural network features for coronary artery disease diagnosis based on cardiac magnetic resonance," *Sci. Rep.*, vol. 12, 2022, Art. no. 11178.

[61] A. Wang, Y. Wang, and Y. Chen, "Hyperspectral image classification based on convolutional neural network and random forest," *Remote Sens. Lett.*, vol. 10, pp. 1086–1094, 2019.

[62] S. Bai, "Growing random forest on deep convolutional neural networks for scene categorization," *Expert Syst. Appl.*, vol. 71, pp. 279–287, 2017.

[63] J. Yang, M. Cai, X. Yang, and Z. Zhou, "Underwater image classification algorithm based on convolutional neural network and optimized extreme learning machine," *J. Mar. Sci. Eng.*, vol. 10, 2022, Art. no. 1841.

[64] D. Su, F. Yang, Y. Ma, X. H. Wang, A. Yang, and C. Qi, "Propagated uncertainty models arising from device, environment, and target for a small laser spot airborne LiDAR bathymetry and its verification in the South China Sea," *IEEE Trans. Geosci. Remote Sens.*, vol. 58, no. 5, pp. 3213–3231, May 2019.

[65] S. Kay, J. D. Hedley, and S. Lavender, "Sun glint correction of high and low spatial resolution images of aquatic scenes: A review of methods for visible and near-infrared wavelengths," *Remote Sens.*, vol. 1, pp. 697–730, 2009.

[66] G. Casal, P. Harris, X. Monteys, J. Hedley, C. Cahalane, and T. McCarthy, "Understanding satellite-derived bathymetry using Sentinel 2 imagery and spatial prediction models," *GISci. Remote Sens.*, vol. 57, pp. 271–286, 2020.

[67] V. Lafon, J. M. Froidefond, F. Lahet, and P. Castaing, "SPOT shallow water bathymetry of a moderately turbid tidal inlet based on field measurements," *Remote Sens. Environ.*, vol. 81, pp. 136–148, 2002.

[68] E. Vahtmäe and T. Kutser, "Airborne mapping of shallow water bathymetry in the optically complex waters of the Baltic Sea," *J. Appl. Remote Sens.*, vol. 10, pp. 025012–025012, 2016.

Jing Zhong received the bachelor's degree in remote sensing science and technology from Chengdu University of Technology, Chengdu, China, in 2021. She is currently working toward the master's degree in surveying and mapping with China University of Geosciences, Wuhan, China.

Her main research interests include marine remote sensing and image classification.

Jie Sun received the Ph.D. degree in photogrammetry and remote sensing from the School of Remote Sensing and Information Engineering, Wuhan University, Wuhan, China, in 2011.

He is currently an Associate Professor with China University of Geosciences, Wuhan, China. His research interests include applications of remote sensing in geology, agriculture, and object recognition.

Zulong Lai received the Ph.D. degree in photogrammetry and remote sensing from Wuhan University, Wuhan, China, in 2011.

He is an Associate Professor with China University of Geosciences, Wuhan, China. His main research interests include land monitoring, pattern recognition, and deformation monitoring.